European Conference on Computational Fluid Dynamics
ECCOMAS CFD 2006
P. Wesseling, E. Oñate and J. Périaux (Eds)


# THE SIMULATION OF VIOLENT FREE-SURFACE DYNAMICS AT SEA AND IN SPACE

**Arthur E.P. Veldman***

*Institute of Mathematics and Computing Science, University of Groningen
P.O. Box 800, 9700AV Groningen, The Netherlands
e-mail: veldman@math.rug.nl
web page: http://www.math.rug.nl/∼veldman/

**Key words:** Free-surface flow, Nonlinear waves, Green water, Dambreak flow, Sloshing, Spacecraft dynamics

**Abstract.** *Non-linear free-surface phenomena, such as extreme waves and violent sloshing, and their impact on the dynamics response of the containing vessels have long been subjects that could only be studied with experimental methods. Nowadays, computational CFD tools can make a significant contribution to these flow problems. The paper starts with a short overview of the most popular numerical methods to simulate highly non-linear free-surface phenomena, with emphasis on Navier–Stokes methods. Thereafter, it describes the development efforts made in the maritime SAFE-FLOW project and the micro-gravity SloshSat FLEVO project. In particular, the improved Volume-of-Fluid (iVOF) free-surface simulation method* ComFlo *is presented. Examples of violent fluid dynamics in both application areas are presented. In all cases experimental data are available to validate the outcome of the calculations.*

## 1 INTRODUCTION

Every-day life shows many examples of free-surface flow: the glass of wine you like to sip or the beautiful surf along the shore in a light sea breeze, to name but a few. However, these flows can also be less romantic, e.g. when the light breeze has strengthened to a heavy storm. In such weather conditions waves can become quite extreme and dangerous. For example, large quantities of 'green' water can come onto the deck of floating and moored structures, presenting a real hazard for both the well-being of the crew and the integrity of the structure[1].

Over the years, several incidents with serious damage have been reported. For instance, in January 2000 the living quarters on the bow of the Varg FPSO were hit by green water, resulting in the damage of a window at the second floor, and flooding the area behind it (Fig. 1). The vessel was out of operation for a number of days. Another example is wave impact damage to the bow of the Schiehallion FPSO in 1998, resulting in an evacuation of the personnel and expensive hull repairs including redesign[2].

Figure 1: Left: Damage and first repair of a window on the Varg FPSO. Right: Artist impression of the NEAR spacecraft.

But also away from our 'blue planet' liquid motion can seriously endanger operations. Everyone over 40 years old will remember the first lunar landing of the Apollo 11 mission. Less well known (but good visible in the video footage) is that shortly before the actual landing, sloshing of the remaining fuel caused an oscillatory motion of the Lunar Module (of about 2-3 degrees), which seriously hampered a safe landing manoeuvre[3]. Another well-documented example is the NEAR (Near Earth Asteroid Rendezvous) mission, where a spacecraft was sent to closely fly-by the Eros asteroid. During the final course correction the spacecraft experienced unexpected motion and went into a safety mode. Ground control was ultimately able to recover the mission, although at the cost of a 13-month delay of the intended rendezvous. Again fuel slosh was named as the probable cause[4].

Thus far, existing analysis methods for free-surface motion largely depend on the application of linear potential flow theory. The physical phenomena accompanying extreme events are highly nonlinear, however, and require new methods as a basis for prediction of the behavior of the water flow. Thus, the desire for simulating complex free-surface problems like slamming, sloshing and the green water phenomenon has been present for a long time[5–7].

The author's research group is involved in a number of projects where the above flow phenomena are studied. Since the late 1970s, together with the National Aerospace Laboratory NLR, theoretical studies are carried out to investigate liquid sloshing on board spacecraft[8–12]. This research has culminated in the design, construction and actual flight of Sloshsat FLEVO, a facility for liquid experimentation in orbit[13]. The project was led by NLR and sponsored by national and international agencies. In the maritime area, the cooperation with MARIN has to be mentioned, leading to the SAFE-FLOW and ComFLOW-2 joint-industry projects. In the present paper we will describe some issues related to the computational modelling of violent free-surface motion in the projects mentioned.

The mathematical model for complex water flow dates from the first half of the 19th century already, known as the Navier–Stokes equations. However, it is only for a decade that these field equations can be solved for large scale complex free-surface flow problems, thanks to novel numerical algorithms and the increase in computer power. This is an

important development; in the near future it should provide, besides model testing, an additional tool for design problems involving these types of flows. This numerical tool is relatively cheap (in comparison with the costs of experimental facilities), therefore it can be used in an early stage of the design process.

The paper will give an impression of the state-of-the art of hydrodynamical methods for describing extremely nonlinear flow. It begins with a short overview of the existing basic methods for complex free-surface flows. Thereafter, the potential is demonstrated of the ComFlo simulation method, which was developed during the above-mentioned cooperations. It is based on the Volume-of-Fluid (VOF) technique, developed by Hirt and Nichols[14]. A number of improvements were found necessary to overcome the weak points of the VOF approach; these are discussed further on in the paper. Originally the method was developed to simulate sloshing liquid on board spacecraft[11,12,15–17]; in this environment capillary forces and contact line dynamics can be quite influential. Later the method was extended to cover applications in maritime engineering[18–20] and biomedical applications[21,22]. Several types of simulations are presented. In the maritime area we show a dambreak flow and a 'green water' event; as an 'extra-terrestrial' example one of the Sloshsat FLEVO manoeuvres is presented. In all examples comparison with experimental data is included.

## 2 METHODS FOR FREE-SURFACE FLOW

To treat dynamically changing, arbitrary liquid configurations a large amount of flexibility has to be present in the numerical approach. It is no longer sufficient to apply a boundary-element philosophy[23,24], but instead a field method has to be used, including a 'bookkeeping' system for tracking the position of the liquid and its free surface[25]. In the literature a number of approaches can be found, of which a short assessment will be given next. A subdivision into three types of methods will be made: fixed-grid methods, moving-grid methods and gridless methods.

### 2.1 Fixed-grid methods

A fixed (or Eulerian) grid to discretise the mathematical model greatly reduces the grid generation effort. However, because the grid is not adapted to the boundaries and free surface, special attention must be paid to capture the position of the free surface and to the implementation of boundary conditions. When an appropriate free-surface tracking/capturing method is used, like Marker-and-Cell (MAC), Volume of Fluid (VOF) or level set, large free-surface deformations can be handled, including fluid splitting and fluid merging.

**MAC and VOF** The Marker-and-Cell (MAC) method is the 'father' of all free-surface flow methods[26], and makes use of massless particles to keep track of the liquid region. Accuracy requires a considerable amount of particles per grid cell, making the method

computationally expensive, especially in 3D. A cheaper way is to apply only surface markers[27], but now splitting and merging of the surface are difficult to handle. The MAC follow up is the Volume-of-Fluid (VOF)[14]. Here a discrete indicator (or color) function is used that corresponds to the cell volume occupied by fluid. Although the original version of the reconstruction and displacement algorithm leads to considerable 'flotsam' and 'jetsam', i.e. artificial drops that numerically pinch off, variants can be designed that can track an arbitrarily moving free surface with high reliability[28,29]. A powerful variant is the piecewise linear reconstruction method (PLIC) introduced by Youngs[30]. Another successful member of this family is the CIP method[31]. An important property of VOF-type methods, resulting from its finite-volume philosophy, is the exact conservation of the amount of liquid present. Various maritime applications of VOF can be mentioned[32–34].

**Level set** An alternative to the indicator-function methods is the level set method[35], which makes use of a function representing the distance to the liquid surface. Reconstruction of the free surface is conceptually simpler than with the VOF method. However, for violently moving free surfaces the level set function requires to be redefined regularly, and conservation of the amount of liquid cannot be guaranteed[36]. Therefore, level set applications mainly focus on relative calm flows, like the steady wave field around ship hulls[37–39]. To reduce mass loss, the level set method is sometimes combined with the VOF method[40,41].

### 2.2 Moving-grid methods

In moving-grid methods, also known as ALE (Arbitrary Lagrangian Eulerian) methods[42], each time step the grid is fitted to the moving free surface in a Lagrangian manner. Their advantage is that the boundaries are well defined, making it easy to apply boundary conditions[43]. However, when the free surface undergoes large deformation, splits or merges, these methods suffer great problems. This makes them less suitable for applications involving complex free-surface flows.

### 2.3 Gridless methods

Gridless methods represent the fluid by a large number of particles. In principle this makes them good methods for problems with large free surface deformations, fluid splitting and fluid merging. The smoothed particle hydrodynamics (SPH) method is an example of such a gridless method. Introduced by Monaghan in an astrophysical context, later applications include the splashing of breaking waves[44], the dam breaking problem[45–47], and the response of floating structures[48]. The application of SPH to fluid dynamics is very young and the method is quite different from other methods, therefore little is known about appropriate numerical boundary conditions (e.g. non-reflecting conditions) and required computational effort (which is still quite large because many particles and small time steps should be used).

## 3 MATHEMATICAL MODEL

**Conservation of mass and momentum** Flow of a homogeneous, incompressible, viscous fluid is described by the continuity equation and the Navier–Stokes equations, describing conservation of mass and momentum, respectively:

$$\oint_{\partial V} \boldsymbol{u} \cdot \boldsymbol{n} \, \mathrm{d}S = 0, \tag{1}$$

$$\int_V \frac{\partial \boldsymbol{u}}{\partial t} \, \mathrm{d}V + \oint_{\partial V} \boldsymbol{u}\boldsymbol{u}^{\mathrm{T}} \cdot \boldsymbol{n} \, \mathrm{d}S = -\frac{1}{\rho} \oint_{\partial V} (p\boldsymbol{n} - \mu \nabla \boldsymbol{u} \cdot \boldsymbol{n}) \, \mathrm{d}S + \int_V \boldsymbol{F} \, \mathrm{d}V. \tag{2}$$

Here $\boldsymbol{u} = (u, v, w)$ denotes the velocity in the three coordinate directions, $\boldsymbol{n}$ is the normal at the boundary $\partial V$ of the control volume $V$, $\rho$ is the density, $p$ is the pressure and $\nabla$ is the gradient operator. Further, $\mu$ denotes the dynamic viscosity and $\boldsymbol{F} = (F_x, F_y, F_z)$ is an external body force like gravity or a virtual body force.

**Boundary conditions** At solid walls a no-slip boundary condition is used: $\boldsymbol{u} = 0$ for fixed boundaries, and $\boldsymbol{u} = \boldsymbol{u}_b$ for moving objects, with $\boldsymbol{u}_b$ being the object velocity. At an inflow boundary the incoming wave is prescribed, e.g. a 5th-order Stokes wave. At the (opposite) outflow boundary a non-reflecting boundary condition is needed. A Sommerfeld condition[49] is appropriate in cases where a regular wave is used. In the case of an irregular wave or a much deformed regular wave (e.g. due to the presence of an object) a damping zone can be added at the end of the domain[20,50,51].

**Free surface** When the position of the free surface is given by $s(\boldsymbol{x}, t) = 0$, its displacement is described by the kinematic condition $Ds/Dt = 0$. At the free surface continuity of normal and tangential stress is prescribed

$$-p + 2\mu \frac{\partial u_n}{\partial n} = -p_0 + \sigma\kappa; \quad \mu \left( \frac{\partial u_n}{\partial t} + \frac{\partial u_t}{\partial n} \right) = 0. \tag{3}$$

Here, $u_n$ and $u_t$ are the normal and tangential component of the velocity respectively, $p_0$ is the atmospheric pressure, $\sigma$ is the surface tension and $\kappa$ denotes the total curvature of the free surface. Further, the angle between the free surface and a solid wall is prescribed; we assume a static contact angle. Experiences with dynamic contact angle models have been described by Van Mourik et al.[15]

## 4 NUMERICAL MODEL – BASICS

### 4.1 Cartesian cut-cell method

To solve the Navier–Stokes equations numerically, the computational domain is covered with a fixed Cartesian grid. The variables are staggered as in the original MAC method[26]: the velocities are defined at cell faces, whereas the pressure is defined in cell centres.

The body geometry is piecewise linear and cuts through the fixed rectangular grid: a cut-cell method[52,53]. Volume apertures ($F^b$) and edge apertures ($A^x$, $A^y$ and $A^z$) are used to indicate for every cell which part of the cell and cell face, respectively, is open for fluid. When moving bodies are present, these apertures are time dependent.

To track the free surface the Volume-of-Fluid function $F^s$ is used, which takes values between 0 and 1, depending on which fraction of the cell is filled with fluid. Cell labelling is introduced to distinguish between cells of different characters (Fig. 2). First the cells that are completely blocked by geometry are called B(oundary) cells. These cells have volume aperture $F^b = 0$. Then the cells that are empty but have the possibility of letting fluid flow in are labelled E(mpty). The adjacent cells containing fluid are S(urface) cells. The remaining cells are labelled as F(luid) cells.

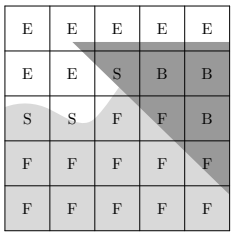


Figure 2: Cell labelling: dark grey denotes solid body, light grey is liquid.

### 4.2 Discretisation of the continuity equation

The continuity and momentum equations are discretised using the finite-volume method starting from the conservative formulation as given in Eqs. (1) and (2). In this paper the discretisation is explained in two dimensions; it can be extended to three dimensions in a straightforward manner. In Fig. 3 a computational F-cell is shown, which is cut by the body geometry. When applying conservation of mass in this cell, the discretisation results in

$$u_e A_e^x \delta y + v_n A_n^y \delta x - u_w A_w^x \delta y - v_s A_s^y \delta x + l(\boldsymbol{u}_b \cdot \boldsymbol{n}_b) = 0, \tag{4}$$

where the notation is explained in Fig. 3 and $\boldsymbol{u}_b = (u_b, v_b)$.

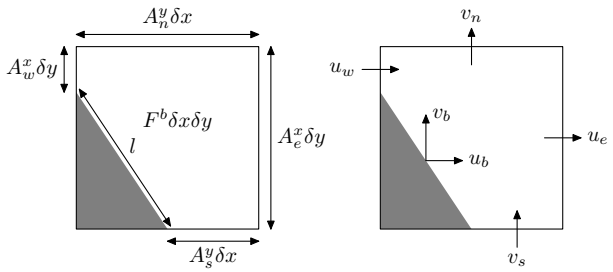


Figure 3: Conservation cell for the continuity equation.

### 4.3 Discretisation of the Navier–Stokes equations

At all faces between cells that contain fluid, i.e. at faces between F-cells and/or S-cells, the Navier–Stokes momentum equations (2) are solved. They are discretised in a control volume around a velocity at a cell face. For uncut cells as well as cut cells, the control volumes are defined as half of the open part of the left neighbour cell plus half of the open part of the right neighbour cell (Fig. 4). The discretisation is explained for the momentum equation in $x$-direction.

The volume integral of the time derivative in Eq. (2) is discretised in space using the midpoint rule. The volume aperture $F_c^b$ of the control volume is defined as $F_c^b = \frac{1}{2}(F_e^b + F_w^b)$ with $F_e^b$ and $F_w^b$ the volume apertures of the eastern and western cell, respectively.

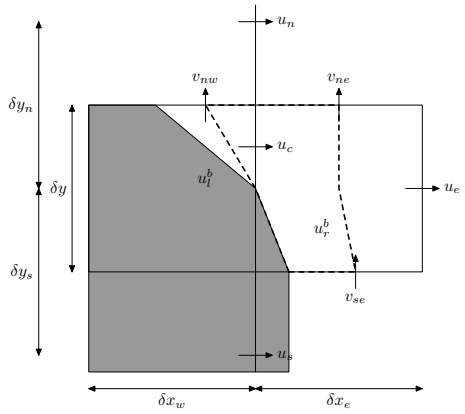


Figure 4: Control volume for the discretisation of convective terms.

The convective boundary integral in Eq. (2) is evaluated at all boundaries of the control volume by multiplying the mass fluxes through the boundaries, $m_r$, $m_d$, $m_l$ and $m_u$ (which are mass fluxes through the right, lower, left and upper boundaries, respectively), with the scalar horizontal velocity $u$ at the respective boundaries. The discretisation is given by

$$\oint_{\partial V} u\,\boldsymbol{u}\cdot\boldsymbol{n}\,\mathrm{d}S \doteq m_r u_r - m_d u_d - m_l u_l + m_u u_u = \\ \tfrac{1}{2}(m_r u_e - m_d u_s - m_l u_w + m_u u_n) + \tfrac{1}{2}(m_r - m_d - m_l + m_u)u_c, \tag{5}$$

with the mass fluxes given by

$$m_r = \tfrac{1}{2}(A_e^x u_e \delta y + A_c^x u_c \delta y + (A_c^x - A_e^x)u_r^b \delta y), \tag{6}$$

$$m_d = \tfrac{1}{2}(A_{se}^y v_{se}\delta x_e + \max(0,(A_{ne}^y - A_{se}^y)v_r^b \delta x_e) \\ + A_{sw}^y v_{sw}\delta x_w + \max(0,(A_{nw}^y - A_{sw}^y)v_l^b \delta x_w)); \tag{7}$$

similar expressions hold for $m_l$ and $m_u$. Here, $A_e^x$ is the aperture belonging to the cell face at which $u_e$ is defined, etc. Note that the mass fluxes consist of a part of the fluid

flow through the open boundaries and a part of the moving body. Inspection learns that the coefficient of the central velocity $u_c$ in Eq. (5) vanishes, making the convective contribution to the coefficient matrix skew symmetric (like the continuous operator), which is a favourable property[54]. Further, artificial diffusion is added such that it transfers the above central discretisation of the convective term into a (more stable) first-order upwind discretisation.

For the diffusive term a discretisation is adopted in which the geometry is handled in a staircase way, so the cut cells are treated as if they are uncut. This has been done to prevent stability problems in small cut cells. In this way, the diffusive discretisation becomes first order, but in the convection-dominated simulations studied here diffusion is not really important[19,20].

The pressure gradient in the $x$-momentum equation is discretised as a boundary integral

$$\oint_{\partial V} p n_x dS \doteq (p_e - p_w) A_c^x \delta y. \tag{8}$$

Here, $p_e$ and $p_w$ are the pressure in the eastern and western cells, respectively (Fig. 4), and $A_c^x$ is the edge aperture of the cell face where the central velocity is defined. Thus the discrete gradient is the negative transpose of the discrete divergence operator Eq. (4), which is also an analytic property[54]. The external force is written as $F_g = -\nabla gz$, and it is discretised similar to the pressure gradient. In this way, it exactly cancels the discrete hydrodynamic pressure.

The equations of motion are discretised in time using the forward Euler method. This first order method is accurate enough, because the order of the overall accuracy is already determined by the first order accuracy of the free-surface displacement algorithm. The pressure is solved from a Poisson equation[55]. It does not require boundary conditions at solid walls; at the free surface the boundary conditions follow from the normal-stress condition in Eq. (3)[26]. Numerical stability of the above time integration puts the usual convective and diffusive requirements on the maximum allowable time step, such as a CFL-condition[16,18–20].

## 5 NUMERICAL MODEL – FREE-SURFACE ISSUES

This section describes some numerical issues concerning the treatment of the free surface: the displacement algorithm and the boundary conditions for the velocity. In particular with respect to these two issues adaptations to the original VOF method have been made.

### 5.1 Free-surface displacement

The free surface is displaced using an improved (iVOF) version of the Volume-of-Fluid method[14]. A piecewise constant reconstruction of the free surface is used, where the free surface is displaced by changing the VOF value in a cell using calculated fluxes through

cell faces. Near the free surface these fluxes are constrained, based on available liquid and/or void space; the original flux expressions[14] are used.

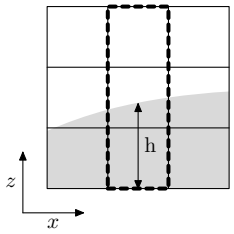


Figure 5: The VOF function in cells near surface cells is updated using a local height function.

The original VOF method has two main drawbacks. The first is that flotsam and jetsam can appear[28,58], which are small droplets disconnecting from the free surface. The other drawback is the gain or loss of water due to rounding the VOF function when $F^s > 1$ or $F^s < 0$. By combining the VOF method with a local height function[16], these problems do not appear any more. For every surface cell locally a function is defined that gives the height of the fluid in a column of three cells (Fig. 5). The direction in which the function is defined is the direction of the coordinate axis that is most normal to the free surface (the positive $z$-direction in Fig. 5). Then, after calculating the fluxes across the cell boundaries of all three cells (the dashed-line region in Fig. 5) as in classical VOF, not the individual VOF values of the three column cells are updated, but the height function is updated. The individual VOF values of the three cells are then calculated from the height of the fluid in the column. In this way, the method is strictly mass conserving and almost no flotsam and jetsam appear[19]. The local height function can also be used to accurately compute the curvature of the free surface[16] (essential for capillary-dominated applications), which has recently led to increasing attention for this approach[56,57].

Both methods, the original VOF method and the iVOF method with local height function, have been compared in a dambreak simulation. In the left Fig. 6 the result is shown of the free surface configuration of a calculation with the original VOF displacement method. The created flotsam and jetsam, small droplets disconnecting from the free surface, are clearly visible. With a local height function, the amount of flotsam and jetsam has decreased considerably as can be seen in the right Fig. 6. Further, the loss of water using original VOF is considerable: about 7% after 6 seconds. In the adapted iVOF method, the loss of water is only 0.02%, so mass is much better conserved.

### 5.2 Velocities near the free surface

Velocities in the neighbourhood of the free surface can be grouped in different classes (see Fig. 2): *i*) the velocities between two F- and/or S-cells are determined from the momentum equation; *ii*) the velocities between an S- and an E-cell are determined using boundary conditions that will be described below; *iii*) the velocities between two E-cells


Figure 6: Snapshots at the end of dambreak flow simulations with different algorithms for the displacement of the free surface: original VOF (left) and VOF combined with a local height function (right).

that are needed to solve the momentum equation are determined using the tangential free-surface condition (3).

The treatment of the velocities at the cell faces between S- and E-cells (SE-velocities) turns out to have significant consequences for the robustness and the accuracy of the simulation method. We discuss two methods, with their respective pro's and con's.

- *Method 1:* The divergence of every S-cell is set to zero as in original MAC[26]. When only one SE-velocity is present in the S-cell, this velocity is uniquely defined. When more E-cells surround the S-cell, the net mass flux through FS-boundaries is divided over the SE-boundaries such that $\nabla \cdot \boldsymbol{u} = 0$ is satisfied.

- *Method 2:* The SE-velocities are determined by extrapolating interior velocities. The velocities used for the extrapolation are taken from the direction of the bulk of the fluid. Both constant and linear extrapolation are considered.

Our simulations reveal that Method 1 gives less accurate results than Method 2. An example can be seen in Fig. 7, where a snapshot of the wave elevation in a steep wave event is shown. The extrapolation of the velocity field of Method 2, indicated by the solid line, gives a good prediction of the wave elevation compared to the measurements.

Further, Method 1 suffers from loss of robustness in cut cells, in particular when the aperture of the SE-velocity is small[19]. However, also linear extrapolation in Method 2 can lead to instabilities when the velocity field is not smooth. But when using constant extrapolation, Method 2 is much more robust.

The smoothness of the pressure field is better for Method 1. When with Method 2 a surface (or empty) cell of which the divergence is not zero (i.e. $\nabla \cdot \boldsymbol{u} \neq 0$) changes into a fluid cell, the pressure has to respond within one time step to restore $\nabla \cdot \boldsymbol{u} = 0$. This shows up as spikes in the pressure signal (see Fig. 10). By construction, these spikes do not appear in Method 1, where always $\nabla \cdot \boldsymbol{u} = 0$ in surface cells.

To overcome the problems described above, in practice a method is chosen that is an engineering mix between the two methods. The extrapolation method with constant extrapolation performs best and has been chosen in our numerical method. But to prevent spikes in the pressure signal, $\nabla \cdot \boldsymbol{u} = 0$ is enforced during each time step when a cell changes

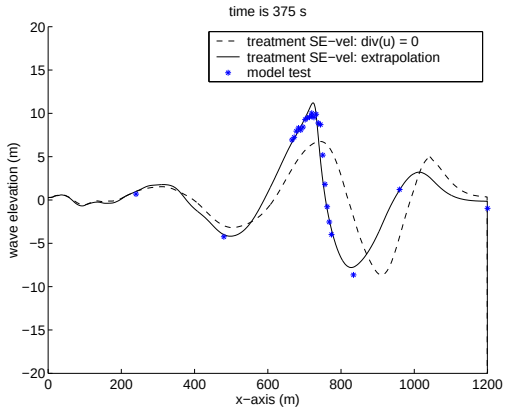


Figure 7: Different methods for free-surface velocities in a steep wave simulation: $\nabla \cdot \boldsymbol{u} = 0$ and linear extrapolation.

label from surface cell to fluid cell. The constant extrapolation is changed to linear extrapolation when greater accuracy in wave simulations is needed. This combination results in a highly accurate and very robust method.

*Remark:* In a two-phase computational model, everywhere in the domain the fluid velocity is calculated[59]; it is always divergence-free. Thus, the ambiguity in selecting conditions for the SE-velocities is circumvented, and the pressure signal is expected to be smooth. First experiences with such an approach do confirm these advantages of a two-phase approach[60,61].

## 6 VALIDATION AND EXAMPLES

### 6.1 Dambreak simulation

At the Maritime Research Institute MARIN experiments have been performed with breaking dam flows. These experiments can be seen as a simple model of green water flow on the deck of a ship. In a large tank of $3.22 \times 1 \times 1\,m^3$, behind a door $0.55\,m$ of water is waiting to be released. In the tank a box has been placed that represents a scale model of a container on the deck of a ship. During the experiment, measurements have been performed of water heights, pressures and forces.

In the simulation, a fine grid of 236×76×68 grid cells has been used with some stretching towards the bottom of the tank. The simulation is continued for 6 seconds with an automatically adapted time step (maximum CFL-number around 0.75), resulting in a time step of the order of 0.001 seconds.

Figure 8 shows a snapshot of the early stage of the simulation together with an image of the video from the experiment. Good agreement between simulation and experiment is observed. The shape of the free surface bending a bit forward is seen in both experiment and simulation. In the simulation the free surface has some ripples, which can be suppressed by using a piecewise linear reconstruction of the free surface[30] instead of the

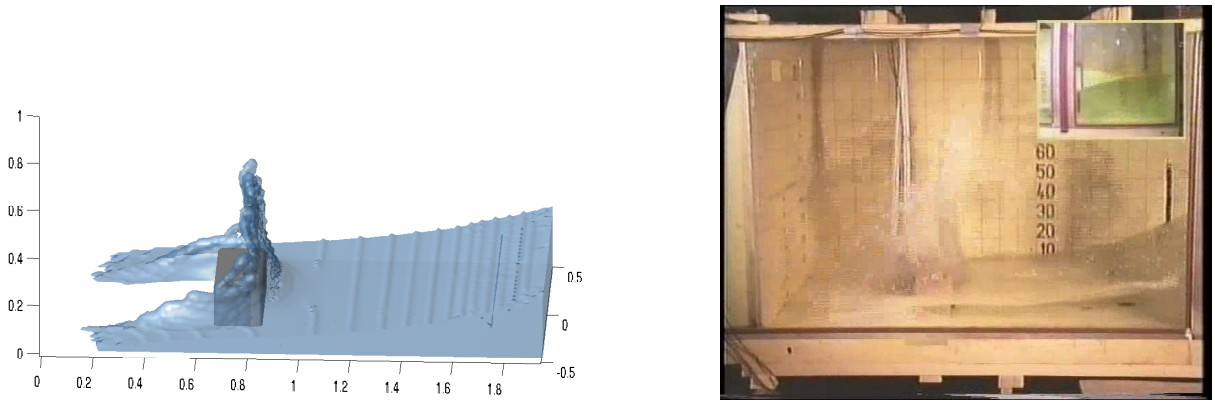


Figure 8: Snapshot of a dambreak simulation with a box in the flow compared with experiment.

reconstruction aligned with the coordinate axes used in this paper.

Figure 9 shows time histories of the water height at two locations: in the reservoir (H4), and in the tank just in front of the box (H2). The agreement in both pictures is very good until the water has returned from the back wall (after about 1.8 seconds). After that some differences occur, but the global behaviour is still the same. After the water has returned from the wall, the fluid height at probe H2 is the largest. The water flows back to the reservoir, where it turns over again after about 4 seconds. The moment that this second wave meets the height probe at H2 again (after about 5 seconds) is almost exactly the same in simulation and experiment.

The instant when the wave hits the box is perfectly captured by the simulation as can be seen from Fig. 10, which shows the pressure at point (P1) at the lower front of the box In this point, the magnitude of the impact pressure is the same for simulation and experiment. The moment the return wave hits the box again (after about 4.7 seconds) is visible in the graphs.

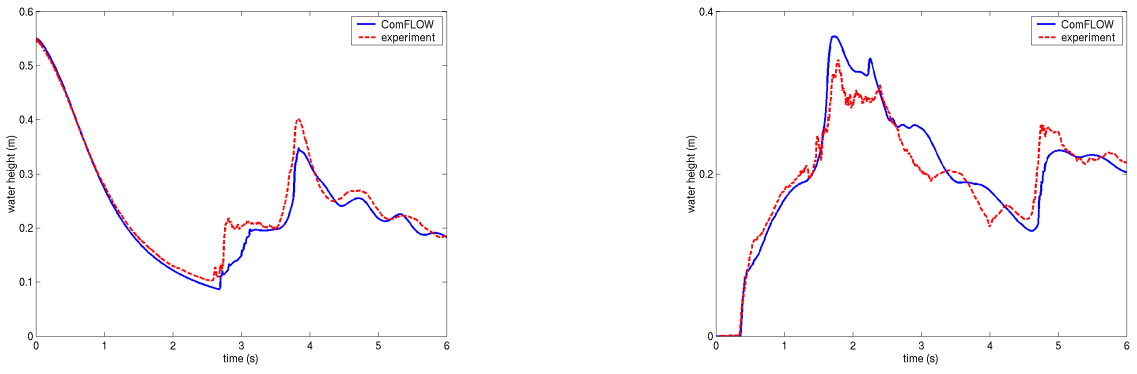


Figure 9: Vertical water heights in the reservoir at position H4 (left) and in the tank at H2 (right).

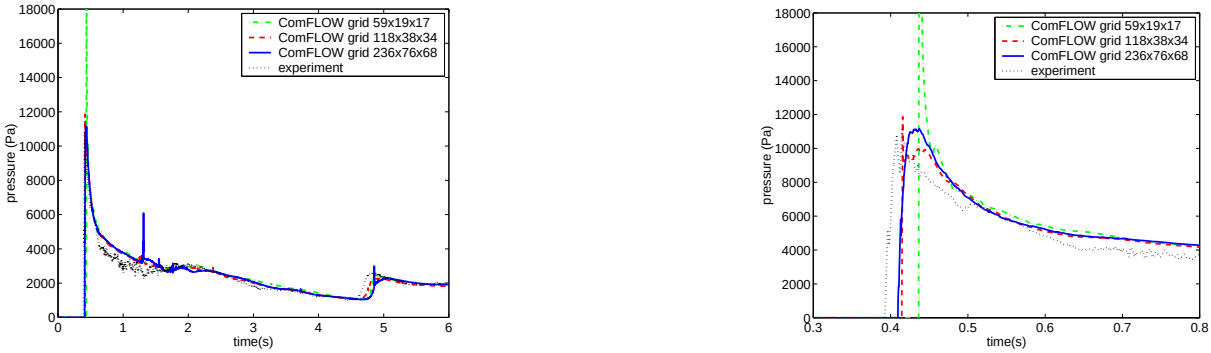


Figure 10: Pressure signals at the lower front of the box (P1) upon grid refinement; the right picture zooms in near first impact.

Some spikes appear in the pressure signals (for example at 1.3 seconds). These spikes occur because some water enters an empty cell that is completely surrounded by cells with fluid. When the water enters the E-cell, there is no empty cell left in the neighbourhood, so this cell changes to a fluid cell in one time step without being a surface cell in between. This discontinuous change in label and the corresponding restoration of $\nabla \cdot \boldsymbol{u} = 0$ results in a pressure peak over the whole pressure field.

Figure 10 also shows a grid refinement study of the dambreak simulation. Three different grids have been used with, in increasing order, $59\times19\times17$, $118\times38\times34$ and $236\times76\times68$ grid points. The pressure along the lower part of the front side of the box is shown. The overall flow of the water is pretty much the same in all three grids, but when zooming in on the pressure peak (in the right-hand figure) differences become visible: the coarsest grid is clearly not good enough.

### 6.2 Green water on deck of moving vessel

As a second application we present a simulation of green water loading using the same wave field characteristics as in an experiment performed by Buchner[5]. Thereto, the computational Navier–Stokes domain is limited to the area close to the bow; the region further away is modelled by a (cheaper) diffraction code (in this case DIFFRAC developed at MARIN). This zonal domain decomposition allows detailed flow simulations in areas with complex nonlinear flows and still limits the computation times. The linear diffraction analysis provides improved boundary conditions (velocities and water heights) for the computational domain, as well as the vessel motion.

In the experiment a free floating FPSO (floating production storage and offloading platform) has been placed in regular waves with period $12.9\,s$, wave height $13.52\,m$ and wavelength $260\,m$; the total water depth is $150\,m$. Measurements were made of the wave in front of the FPSO, water heights and pressures at the deck and the pressure at some places on a deck structure.

The grid on which the kinematics are calculated in the diffraction code consists of

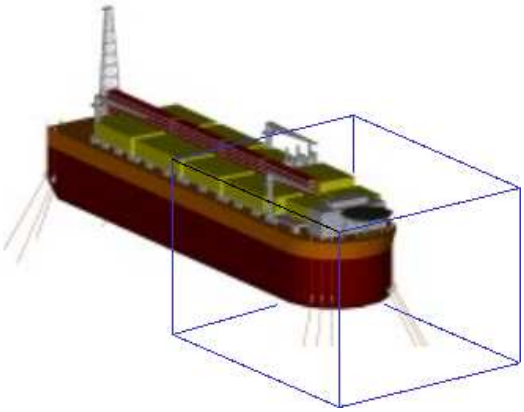

Figure 11: Zonal domain decomposition: the Navier–Stokes calculations are restricted to the surroundings of the bow, the far-field wave kinematics and vessel motions are calculated using a diffraction code.

$61 \times 21 \times 13$ grid points with a distance between the grid points of $13\,m$, $13\,m$ and $12.5\,m$ in $x$-, $y$- and $z$-direction, respectively. The computational domain is focussed on the bow of the ship, and covers about half a wavelength up front and half the ship length aft of the bow. The $y$-coordinate has values between $-100$ and $100\,m$, whereas in $z$-direction the domain is cut off at $-100\,m$. Selecting a grid for such computations is always a compromise between accuracy, computer memory and computing time. A grid of $112 \times 80 \times 76$ grid points is used in the iVOF simulation with stretching towards the bow of the ship: cells in the neighbourhood of the bow have sizes in $x$-, $y$- and $z$-direction of $1.4\,m$, $2.0\,m$ and $1.1\,m$, respectively. The simulation has been carried out for 15 seconds. The discrete treatment of the latter motion relative to the fixed Cartesian grid is described in detail in the PhD theses of Fekken[18] and Kleefsman[20].

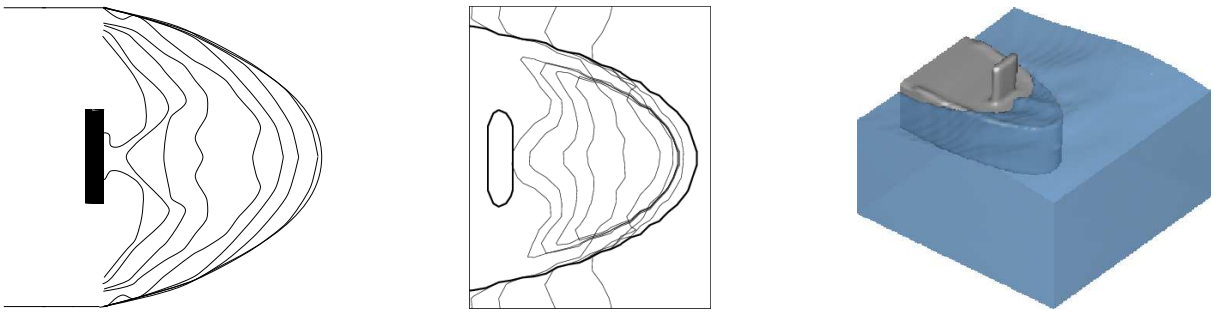

Figure 12: Contours of the water front propagating over the deck of the FPSO, model test every $0.31\,s$ (left) and ComFlo every $0.30\,s$ (middle). Right: snapshot of the simulation.

Figure 12 shows contours describing the propagation of the water front on the deck of the FPSO. The agreement between the propagation of the water front in experiment and simulation is rather good. The water jet is formed a bit earlier in the simulation than in the experiment. Also, a snapshot of the simulation at time $7.5\,s$ is shown, where the high velocity jet is very well visible.

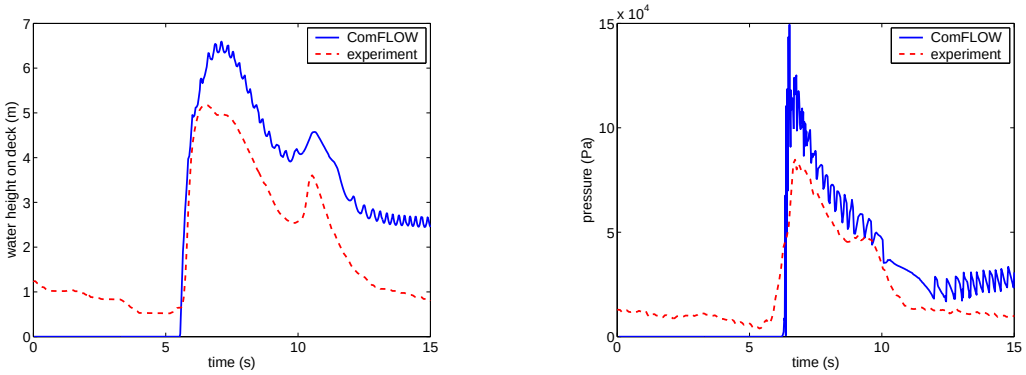


Figure 13: Water height (left) and pressure (right) at the deck close to the deck structure.

Figure 13 shows water height and pressure at a position close to the deck structure. The predicted water height is 1.5 meter higher than measured in the experiment; however, note that this difference is less than two grid cells. The second hump in the left of Fig. 13 is predicted by ComFlo at the same moment as in the experiment. This hump is present due to the water returning from the deck structure. The right-hand graph in Fig. 13 shows the pressure; again the amount of water on the deck is too large. In this graph, an oscillating behaviour of the pressure can be observed, which as caused because the monitoring point, fixed at the moving structure, switches to another computational cell.

### 6.3 Sloshing in micro-gravity

A third example of free-surface flow concerns sloshing liquid on board spacecraft. Experiments have been carried out recently with the Sloshsat FLEVO spacecraft, launched on February 12, 2005. This mini satellite has been built by the Dutch National Aerospace Laboratory NLR[13]. Its dry mass is 95 kg. A cylindrical shaped fluid tank with hemispherical ends, with a volume of 86.9 liters, is positioned inside the satellite. This tank is partly filled with 33.5 kg of distilled water, which could freely slosh during the experiments. Given the physical properties of the tank material, a contact angle of 90 degrees is considered a reasonable assumption. The motion of Slsohsat is controlled by 12 thrusters. During a period of 8 days various experiments have been carried out; several relevant quantities for the Sloshsat motion were measured, such as the angular velocity $\boldsymbol{\omega}$ and the linear acceleration $\dot{\boldsymbol{q}}$. The various experiments and preliminary results are described by Vreeburg[10] and Luppes et al.[11,12].

The experiments with Sloshsat were supported by a theoretical/computational model implemented in ComFlo, combined with a model for coupled solid-liquid interaction dynamics[16,17]. The latter influence is modelled as a virtual body force $\boldsymbol{F}$ in the Navier–Stokes momentum equation (2):

$$\boldsymbol{F} = -\dot{\boldsymbol{q}} - \dot{\boldsymbol{\omega}} \times \boldsymbol{r} - \boldsymbol{\omega} \times (\boldsymbol{\omega} \times \boldsymbol{r}) - 2\boldsymbol{\omega} \times \boldsymbol{u}, \tag{9}$$

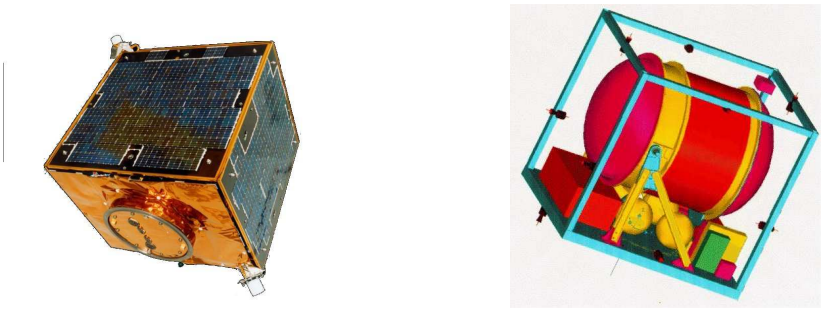

Figure 14: The Sloshsat FLEVO satellite: left the exterior; right a schematic internal view.

where $\dot{\boldsymbol{q}}$ denotes the linear acceleration of the moving coordinate frame fixed to the solid body, and $\boldsymbol{\omega}$ and $\dot{\boldsymbol{\omega}}$ denote the angular velocity and acceleration of the solid body.

In this paper we will present some results for a so-called flat-spin manoeuvre. Here, Sloshsat is initially forced to rotate around the axis of intermediate MOI (moment of inertia), during which the fluid configuration settles in equilibrium. After some time, the thruster action is canceled and a free tumble of Sloshsat commences. During this free tumble, the rotational direction of Sloshsat (slowly) moves towards the maximum MOI, with a significant amount of nutation and large-scale fluid action. Hence, such a manoeuvre is very suitable for the validation of our numerical model.

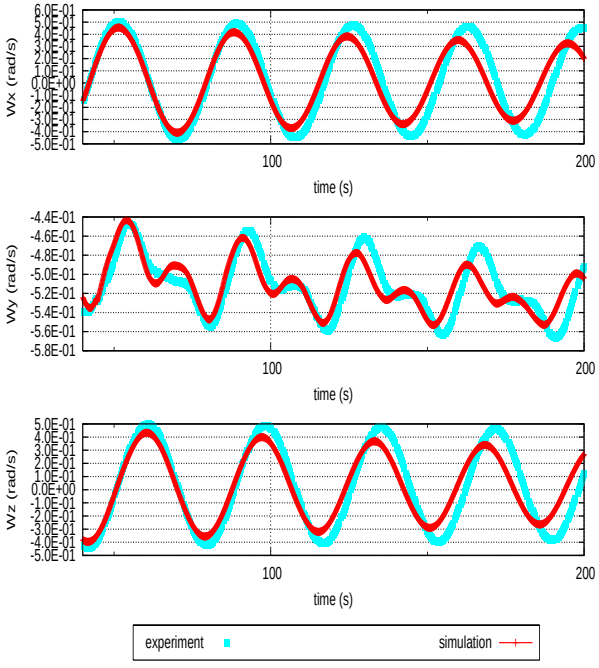


Figure 15: Simulation versus measurements for the flat-spin experiment.

The comparison for the flat-spin manoeuvre is given in Fig. 15. Controlled by thruster action, in the first 33 seconds Sloshsat is approximately rotating around the axis of in-

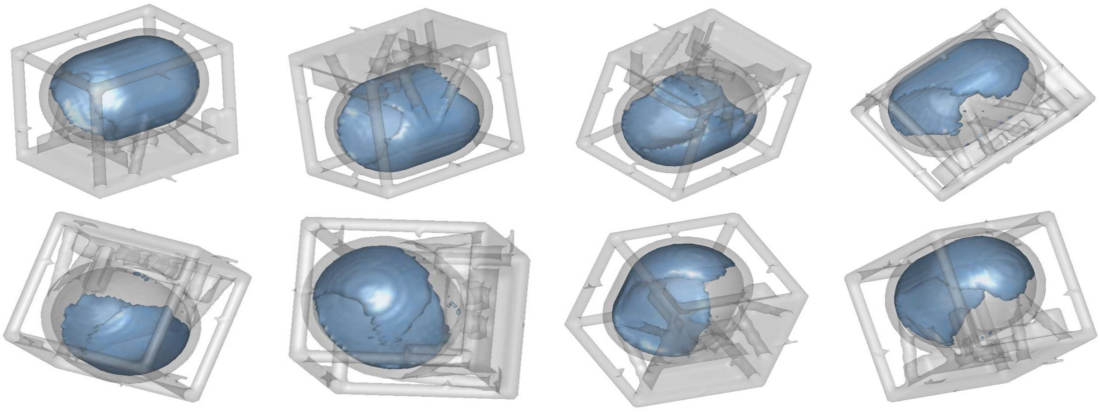

Figure 16: Sloshsat orientation and water configuration during a flat-spin manoeuvre at $t = 14$, 18, 32, 37, 44, 64, 830 and 831 seconds. (lexicographical order).

termediate MOI. Then the thruster action is stopped, and Sloshsat is allowed to tumble freely. The obtained components of $\boldsymbol{\omega}$ of the simulation are in good agreement with those of the measurements, except for a higher level of damping (which is due to some numerical diffusion). The profile of $\boldsymbol{\omega}_y$ shows an interesting phenomenon. Each nutation period contains a higher frequency, which is the result of sloshing water pounding the tank wall. This secondary frequency is present in both experiment and simulation, indicating that in the simulation the Sloshsat motion adopts the sloshing frequency correctly.

The Sloshsat orientation and water configuration during the simulation of the flat-spin manoeuvre is depicted in Fig. 16. In the first subfigure, the water inside Sloshsat is adapted to the rotation around the axis of intermediate MOI ($t = 14s$). In the next figures, the fluid movement during the free tumble manoeuvre is shown. In the two final subfigures, the transition toward stable rotation around the axis of maximum MOI is almost completed ($t = 830s$ and $831s$). The orientation in these subfigures indicates a rotation period of $T \approx 12$ seconds, which is in agreement with $\boldsymbol{\omega}_y \approx -0.55$ (Fig. 15).

## 7 CONCLUDING REMARKS

In the present paper results have been shown of the simulation of hydrodynamic impact problems using the iVOF Navier–Stokes solver ComFlo. The combination of the original VOF method with a local height function considerably improves the free-surface treatment by removing much of the flotsam and jetsam. Also, the sensitivity of the simulation results to the boundary conditions for the velocities at the free surface has been discussed.

Engineering applications have been presented for a dambreak flow, green water on a moving vessel, and sloshing in a spacecraft. In all cases experimental data are available for validation purposes.

• The dambreak simulation featured an on-deck box on which pressures and forces have been measured and calculated. The comparison with experiment was found very good.

• In the green water simulation a zonal domain decomposition has been applied: the far

field has been described by a (cheaper) diffraction method, and only the close vicinity is modelled with the (more expensive) nonlinear Navier–Stokes equations. Pressure loads on the deck structure compare quite well with experiment, although the amount of water on deck is somewhat overpredicted.
• The flat-spin example includes capillary physics as well as liquid–spacecraft interaction. It shows that the sloshing frequency of the water inside the tank is adopted correctly by the satellite motion, although the damping is somewhat overpredicted.

The results of the simulations give much confidence in the performance of the method. It will be developed further in the coming years by extending it towards compressible two-phase flows (in the ComFLOW-2 project[61]). A major advantage of a two-phase model is that the boundary conditions for the velocities at the free surface, which have a large influence on the robustness and accuracy of the method, are not needed anymore. Also, in this way pockets of entrapped air in the wave impact region can be modelled; these can have a substantial influence on the impact pressures[62,63].

## ACKNOWLEDGEMENTS

The paper describes the efforts of the ComFlo development team at the University of Groningen, which operates in close cooperation with the Maritime Research Institute MARIN, FORCE Technology (Norway), Delft University of Technology, and the National Aerospace Laboratory NLR. In particular, the author would like to acknowledge the contributions of (in alphabetical order) Geert Fekken, Jeroen Gerrits, Joop Helder, Theresa Helmholt-Kleefsman, Erwin Loots, Roel Luppes and Rik Wemmenhove at the University of Groningen; Bas Buchner, Tim Bunnik and Arjan Voogt at MARIN; Erik Falkenberg and Bogdan Iwanowski at FORCE Technology; Jo Pinkster and Peter Wellens at TU Delft; and, last but not least, Koos Prins and Jan Vreeburg at NLR.

The maritime part of the presented research has been carried out in the SAFE-FLOW project (SAFE-FLOating offshore structures under impact loading of shipped green water and Waves), funded by the European Community under the 'Competitive and Sustainable Growth' Programme (EU Project No.: GRD1-2000-25656) and a group of 26 industrial participants. The author is solely responsible for the present paper and it does not represent the opinion of the European Community. The ComFLOW-2 joint industry project is co-funded by the Dutch Technology Foundation STW.
The micro-gravity part of the presented research has been supported by the National Institute for Space Research in the Netherlands (SRON; project MG-065). The Sloshsat FLEVO project is a harmonised programme between the European Space Agency (ESA) and the Netherlands Agency for Aerospace Programs (NIVR) with NLR as main contractor.

## REFERENCES

[1] W.D.M. Morris, J. Millar and B. Buchner. Green water susceptibility of North Sea FPSO/FSUs. In: *Proc. 15th Conf. on Floating Production Systems (FPS)*, London (2000).

[2] P. Gorf, N. Barltrop, B. Okan, T. Hodson and R. Rainey. FPSO bow damage in steep waves. In: *Proc. Rogue Waves*, Brest (2000).

[3] Apollo 11 Lunar Surface Journal. *The first lunar landing.* See 102:38:20 mission time. Available at `http://www.hq.nasa.gov/office/pao/History/alsj/a11/a11.landing.html`

[4] NEAR Anomaly Review Board. *The NEAR Rendezvous burn anomaly of December 1998.* Johns Hopkins University, Applied Physics Laboratory (November 1999).

[5] B. Buchner. *Green water on ship-type offshore structures.* PhD thesis, Department of Maritime Technology, Delft University of Technology (2002).

[6] O.M. Faltinsen. *Sea Loads on Ships and Offshore Structures.* Cambridge University Press (1999).

[7] B. Molin and J. Ferziger. Hydrodynamique des structures offshore. *Appl. Mech. Rev.*, **56**, B29 (2003).

[8] A.E.P. Veldman and M.E.S. Vogels. Axisymmetric liquid sloshing under low gravity conditions. *Acta Astronautica* **11**, 641–649 (1984).

[9] J.P.B. Vreeburg and A.E.P. Veldman. Transient and sloshing motions in an unsupported container. In: R. Monti (ed.) *Physics of Fluids in Microgravity.* Taylor and Francis Publishers, pp. 293–321 (2002).

[10] J.P.B. Vreeburg. Measured states of SLoshsat FLEVO. In: *Proc. 56th Int. Astronaut. Congr.*, Fukuoka, Japan, Paper IAF-05-C1.2.09 (2005).

[11] R. Luppes, J.A. Helder and A.E.P. Veldman. Liquid sloshing in microgravity. In: *Proc. 56th Int. Astronaut. Congr.*, Fukuoka, Japan, Paper IAF-05-A2.2.07 (2005).

[12] R. Luppes, J.A. Helder and A.E.P. Veldman. The numerical simulation of liquid sloshing in microgravity. In: *Proc. ECCOMAS CFD 2006,* Egmond aan Zee, Netherlands (2006).

[13] J.J.M. Prins. Sloshsat FLEVO: Facility for liquid experimentation and verification in orbit. In: *Proc. 51st Int. Astronaut. Congr.*, Paper IAF-00-J.2.05 (2000).

[14] C.W. Hirt and B.D. Nichols. Volume of fluid (vof) method for the dynamics of free boundaries. *J. Comp. Phys.*, **39**, 201–225 (1981).

[15] S. van Mourik, A.E.P. Veldman and M. Dreyer. Simulation of capillary flow with a dynamic contact angle. *Microgravity Sci. Technol.*, **17**(3), 87–94 (2005).

[16] J. Gerrits. *Dynamics of liquid-filled spacecraft.* PhD thesis, University of Groningen (2001).

[17] J. Gerrits and A.E.P. Veldman. Dynamics of liquid-filled spacecraft. *J. Eng. Math.*, **45**, 21–38 (2003).

[18] G. Fekken. *Numerical simulation of free-surface flow with moving rigid bodies.* PhD thesis, University of Groningen (2004).

[19] K.M.T. Kleefsman, G. Fekken, A.E.P. Veldman, B. Iwanowski and B. Buchner. A Volume-of-Fluid based simulation methods for wave impact problems. *J. Comp. Phys.*, **206**, 363–393 (2005).

[20] K.M.T. Kleefsman. *Water impact loading on offshore structures - a numerical study.* PhD thesis, University of Groningen (2005).

[21] E. Loots, B. Hillen and A.E.P. Veldman. The role of hemodynamics in the development of the outflow tract of the heart. *J. Eng. Math.*, **45**, 91–104 (2003).

[22] N.M. Maurits, G.E. Loots and A.E.P. Veldman. The influence of vessel wall elasticity and peripheral resistance on the flow wave form: a CFD model compared to in-vivo ultrasound meaurements. *J. Biomech.*, available online February 2006.

[23] R.W. Yeung. Numerical methods in free-surface flows. *Ann. Rev. Fluid Mech.*, **12**, 395–442 (1982).

[24] W. Tsai and D.K.P. Yue. Computation of nonlinear free-surface flows. *Ann. Rev. Fluid Mech.*, **28**, 249–278 (1996).

[25] R. Scardovelli, S. Zaleski. Direct numerical simulation of free-surface and interfacial flow, *Ann. Rev. Fluid Mech.*, **31**, 567–603 (1999).

[26] F.H. Harlow and J.E. Welch. Numerical calculation of time-dependent viscous incompressible flow of fluid with free surface. *Phys. Fluids*, **8**, 2182–2189 (1965).

[27] D. Juric and G. Tryggvason. A front tracking method for dendritic solidification, *J. Comp. Phys.*, **123**, 127–148 (1996).

[28] W.J. Rider and D.B. Kothe. Reconstructing volume tracking. *J. Comp. Phys.*, **141**, 112–152 (1998).

[29] M. Rudman. Volume-tracking methods for interfacial flow calculations, *Int. J. Numer. Meth. Fluids*, **24**, 671–691 (1997).

[30] D.L. Youngs. *An interface tracking method for a 3D Eulerian hydrodynamics code*, Technical Report AWRE/44/92/35, Atomic Weapons Research Establishment, 1987.

[31] T. Yabe, F. Xiao and T. Utsumi. The constrained interpolation profile method for multiphase analysis. *J. Comp. Phys.*, **169**, 556–593 (2001).

[32] M. Greco, O.M. Faltinsen and M. Landrini. Numerical simulation of heavy water shipping. In: *Proc. 17th Workshop on Water Waves and Floating Bodies*, Cambridge UK, 14-16 April 2002.

[33] Y. Kim. Numerical simulation of sloshing flows with impact load. *Appl. Ocean Res.*, 23, 53–62 (2001).

[34] S. Muzaferija, M. Peric, P. Sames and T. Schellin. A two-fluid Navier–Stokes solver to simulate water entry. In: *Proc. 22nd Symp. Naval Hydrodynamics*, pp. 638-649 (2001).

[35] J.A. Sethian. *Level Set Methods: Evolving Interfaces in Geometry, Fluid Mechanics, Computer Vision and Materials Science.* Cambridge University Press (1996).

[36] W.J. Rider and D.B. Kothe. Stretching and tearing interface tracking methods. *AIAA paper 95-1717* (1995).

[37] F. Bet, D. Hänel, and S. Sharma. Numerical simulation of ship flow by a method of artificial compressibility. In: *Proc. 22th Symp. Naval Hydrodynamics*, page 173 (1998).

[38] M. Sussman and D. Dommermuth. The numerical simulation of ship waves using cartesian grid methods. In: *Proc. 23th Symp. Naval Hydrodynamics*, pp. 762–779 (2001).

[39] A. Iafrati, A. Di Mascio, E.F. Campana. A level set technique applied to unsteady free surface flows. *Int. J. Numer. Methods Fluids*, **35**, 281–297 (2001).

[40] M. Sussman and E.G. Puckett. A coupled level set and volume-of-fluid method for computing 3d and axisymmetric incompressible two-phase flows. *J. Comp. Phys.*, **162**, 301–337 (2000).

[41] S. van der Pijl. *Computation of bubbly flows with a mass-conserving level-set method.* PhD thesis, TU Delft (2005).

[42] C.W. Hirt, A.A. Amsden and J.L. Cook. An arbitrary Lagrangian-Eulerian method for all flow speeds. *J. Comp. Phys.*, **14**, 227–253 (1974).

[43] B. Alessandrini and G. Delhommeau. A fully coupled Navier–Stokes solver for calculation of turbulent incompressible free surface flow past a ship hull. *Int. J. Num. Meth. Fluids*, **29**, 125–142 (1999).

[44] M.P. Tulin and M. Landrini. Breaking waves in the ocean and around ships. In: *Proc. 23th Symp. Naval Hydrodynamics*, pp. 713–745 (2001).

[45] J.J. Monaghan. Simulating Free Surface Flows with SPH. *J. Comp. Phys.*, **110**, 399–406 (1994).

[46] Y. Andrillon, M. Doring, B. Alessandrini, and P. Ferrant. Comparison between sph and vof free surface flow simulation. In: *Proc. 5th Numerical Towing Tank Symposium* (2002).

[47] A. Colagrossi and M. Landrini. Numerical simulations of 2-phase flows by smoothed particle hydrodynamics. In: *Proc. 5th Numerical Towing Tank Symposium* (2002).

[48] H. Maeda, K. Nishimoto, K. Masuda, T. Asanuma, M.M. Tsukamoto and T. Ikoma. Numerical analysis for hydrodynamic motions of floating structure using MPS method. In: *Proc. 23rd Int. Conf. Offshore Mech. Arctic Eng.*, Vancouver, June 20-25 (2004).

[49] I. Orlanski. A simple boundary condition for unbounded hyperbolic flows. *J. Comp. Phys.*, **21**, 251–269 (1976).

[50] A. Clément. Coupling of two absorbing boundary conditions for 2D time-domain simulations of free surface gravity waves. *J. Comp. Phys.*, **126**, 139–151 (1996).

[51] M. Israeli, S.A. Orszag. Approximation of radiation boundary conditions. *J. Comp. Phys.*, **41**, 115–135 (1981).

[52] G. Yang, D.M. Causon and D.M. Ingram. Calculation of compressible flows about complex moving geometries using a Cartesian cut cell method. *Int. J. Num. Meth. Fluids*, **33**, 1121–1151 (2000).

[53] M. Dröge and R. Verstappen. A new symmetry-preserving Cartesian-grid method for computing flow past arbitrarily shaped objects. *Int. J. Num. Meth. Fluids*, **47**, 979–985 (2005).

[54] R.W.C.P. Verstappen and A.E.P. Veldman, Symmetry-preserving discretisation of turbulent flow. *J. Comp. Phys.*, **187**, 343–368 (2003).

[55] E.F.F. Botta and M.H.M. Ellenbroek. A modified SOR method for the Poisson equation in unsteady free-surface flow calculations. *J. Comp. Phys.*, **60** 119-134 (1985).

[56] S.J. Cummins, M.M. Francois and D.B. Kothe. Estimating curvature from volume fractions. *Comput. Struct.*, **83**, 425–434 (2005).

[57] M.M. Francois, S.J. Cummins, E.D. Dendy, D.B. Kothe, J.M. Sicilian and M.W. Williams, A balanced-force algorithm for continuous and sharp interfacial surface tension models within a volume tracking framework. *J. Comp. Phys.*, **213**, 141–173 (2006).

[58] D.J.E. Harvie and D.F. Fletcher. A new volume of fluid advection algorithm: the stream scheme. *J. Comp. Phys.*, **162**, 1–32 (2000).

[59] S.J. Osher and G. Tryggvason (eds.) Special issue on 'Computational methods for multiphase flows'. *J. Comp. Phys.* **169**, 249–759 (2001).

[60] R. Wemmenhove, E. Loots, R. Luppes and A.E.P. Veldman. Modelling two-phase flow with offshore applications. In: *Proc. 24th Int. Conf. Offshore Mech. Arctic Eng.*, Halkidiki, Greece, paper OMAE2005-67460 (2005).

[61] R. Wemmenhove, E. Loots and A.E.P. Veldman. Numerical simulation of hydrodynamic wave loading by a compressible two-phase model. In: *Proc. ECCOMAS CFD 2006*. Egmond aan Zee, Netherlands (2006).

[62] D.H. Peregrine and L. Thais. The effect of entrained air in violent water wave impacts. *J. Fluid Mech.*, **325**, 377–397 (1996).

[63] J.H. Duncan. Spilling breakers. *Ann. Rev. Fluid Mech.*, **33**, 519–547 (2001).